Computational Efficient Parameter and Performance Prediction of Wound-Rotor Induction Motor

Mkhululi Mabhula and Maarten J. Kamper

Department of Electrical and Electronic Engineering, Stellenbosch University, Stellenbosch 7600, South Africa

A basic, fast, and accurate steady-state finite-element analysis (FEA) based parameter and performance calculation method for the wound-rotor induction motor is presented. The method couples the circuit equations with field equations using the principle of frozen permeabilities to present the voltage-fed induction motor. The effects of saturation saliency and cross-magnetization are accurately taken into account. The method is verified by direct comparison with the current- and torque-slip frequency curves obtained from a commercial FEA package.

Index Terms— **Cross-coupling, finite-element analysis (FEA), flux linkages, two-axis modeling, wound-rotor induction motor (WR-IM).**

I. Introduction

LARGE power wound-rotor induction motors (WR-IMs) are still one of the common motor loads on the grid, widely used for high locked rotor torque and low startup currents [1]–[4]. Hence, fast and accurate parameter determination of the WR-IM is of topical interest; with these parameters, the performance characteristics can be determined for the optimum design of the motor [5]–[10].

The main drawback is the complex analysis of the WR-IM because of the existence of alternating currents in both stator and rotor of the motor. The finite-element (FE) analysis (FEA) method is a broadly used, very accurate numerical method for motor performance determination [11]–[16]. The time-stepping FEA method has been used for the accurate determination of the transient performance of the IM [3], [5], [17]–[19]. However, the method is not computationally time efficient for steady-state analysis and machine design optimization.

Lately, the time-harmonic (TH) FEA method, mainly applied to squirrel-cage induction motors, has been widely used for strict computation of the motor performance [18], [20]–[23]. The major drawback of the stated TH method is that only the linear region of the motor is considered and that is also time consuming especially when only steady-state performance is needed. Mezani *et al.* [16] successfully use the truncated version of the TH method [23], [24] for the first time on the computation of the WR-IM. In [16], the double air-gap method is used, only considering the principal air-gap space-harmonic of the magnetic flux in which only four FE magnetostatic computations are required to determine the WR-IM performance for any slip value. The disadvantage of this method is that only the linear case or in average non-linear case is considered [23]. The accuracy of the proposed method of Mezani *et al.* [16] has proved not always to be, essentially on the torque prediction.

Manuscript received September 11, 2017; revised November 27, 2017 and January 29, 2018; accepted February 6, 2018. Date of publication March 14, 2018; date of current version May 16, 2018. Corresponding author: M. J. Kamper (e-mail: kamper@sun.ac.za).

Color versions of one or more of the figures in this paper are available online at http://ieeexplore.ieee.org.

Digital Object Identifier 10.1109/TMAG.2018.2807394

Instead of considering the first space-harmonic air-gap magnetic flux proposed in [16], the total overall flux linkage of the motor produced by the three phases is considered in this paper for parameter and performance calculation. A simple and basic FE parameter and performance prediction method recommended for the design optimization of WR-IM is newly introduced. With this method not only the linear case but also the saturation saliency and cross-coupling effects on the motor parameters incorporating all leakage flux linkages are considered. A proof is given on the extreme fastness and accuracy of the method in performance prediction.

II. Flux Linkage Computation of WR-IM

In the total flux linkage computation, the field is assumed not changing in the z-axis. Thus, the 2D FE solution magnetic vector potential has only the z-directed component, i.e.,

$$\mathbf{A} = A_z \mathbf{z} \tag{1}$$

where $\mathbf{z}$ is the z-directed unit vector. The net total flux linkage of a winding through a surface S is calculated using the relation $\mathbf{B} = \nabla \times \mathbf{A}$ and Stoke's theorem as

$$\varphi = \int_S \mathbf{B} \cdot d\mathbf{S} = \int_S (\nabla \times \mathbf{A}) \cdot d\mathbf{S} = \oint_C \mathbf{A} \cdot d\mathbf{l}. \tag{2}$$

Considering (2) for a coil area S divided into n first-order triangle mesh FEs, N turns and length l along the z-direction, the flux linkage of a coil is

$$\lambda = N\varphi = N \sum_{j=1}^{n} \frac{\boldsymbol{\Delta}_j}{S} \left(\Im \frac{1}{3} \sum_{i=1}^{3} \mathbf{A}_{ij} \right) l. \tag{3}$$

In (3), $\mathbf{A}_{ij}$ is the magnetic vector potential of nodal point $i = 1$, $i = 2$, or $i = 3$ of the jth triangular element of area $\boldsymbol{\Delta}_j$. The direction of the integral either into or out of a plane is given by $\Im$ (i.e., $+1$ or -1). Considering (3) and one meshed pole, the net total flux linkage of a phase winding can be expressed as

$$\lambda_{\text{abc}} = \frac{2pNl}{S} \sum_{j=1}^{u} \left(\frac{\boldsymbol{\Delta}_j \Im}{3} \sum_{i=1}^{3} \mathbf{A}_{ij} \right) \tag{4}$$

where u is the total number of elements of the meshed coil areas of the phase in the pole region [25]. The total net flux linkage of (4) includes high-order harmonic and leakage fluxes produced by the winding, slotted air gap, and magnetic saturation. The total flux linkage is essential because with that a complete parameter and performance (e.g., power factor) prediction model of the motor can be obtained.

III. Electromagnetic Model of WR-IM

The stator and rotor voltages are classically expressed as

$$\mathbf{v}_{\text{abc}_{(s,r)}} = \mathbf{R}_{(s,r)}\mathbf{i}_{\text{abc}_{(s,r)}} + \frac{d}{dt}\boldsymbol{\lambda}_{\text{abc}_{(s,r)}} \tag{5}$$

where $R_{(s,r)}$ given by

$$R_{(s,r)} = (\rho_{cu})_t \frac{l_{T_{(s,r)}} N_{(s,r)}^2 pq}{A_{cu_{(s,r)}}} \qquad l_{T_{(s,r)}} = 2(l + l_{e_{(s,r)}}) \tag{6}$$

and $\boldsymbol{\lambda}_{\text{abc}_{(s,r)}}$ of (4) are stator or rotor phase resistances and flux linkages. In (6), $A_{cu_{(s,r)}}$ and $(\rho_{cu})_T$ are the copper slot cross-sectional area and resistivity at temperature T, respectively. The total conductor length l_T of (6) is the sum of stack length l and end-winding length l_e given by Boldea and Nasar [11]. $N_{(s,r)}$ and q are the number of turns per slot and slots per pole per phase, respectively. The balanced three voltage, current, and flux linkage phases of (5), representing a stationary time-dependent system, are transformed to a rotating time-dependent system (DQ-axis) and inverse transformed as

$$\mathbf{v}_{dq_{(s,r)}} = \mathbf{T}(\theta_{(s,r)})\mathbf{v}_{\text{abc}_{(s,r)}}; \quad \mathbf{v}_{\text{abc}_{(s,r)}} = \mathbf{T}^{-1}(\theta_{(s,r)})\mathbf{v}_{dq_{(s,r)}} \tag{7}$$

$$\mathbf{i}_{dq_{(s,r)}} = \mathbf{T}(\theta_{(s,r)})\mathbf{i}_{\text{abc}_{(s,r)}}; \quad \mathbf{i}_{\text{abc}_{(s,r)}} = \mathbf{T}^{-1}(\theta_{(s,r)})\mathbf{i}_{dq_{(s,r)}} \tag{8}$$

$$\boldsymbol{\lambda}_{dq_{(s,r)}} = \mathbf{T}(\theta_{(s,r)})\boldsymbol{\lambda}_{\text{abc}_{(s,r)}}; \quad \boldsymbol{\lambda}_{\text{abc}_{(s,r)}} = \mathbf{T}^{-1}(\theta_{(s,r)})\boldsymbol{\lambda}_{dq_{(s,r)}} \tag{9}$$

where $\mathbf{T}$ and $\mathbf{T}^{-1}$ are transformation matrices expressed in terms of the electrical rotor position angle (transformation angle) θ given in matrix form as

$$\mathbf{T} = \begin{bmatrix} \cos\theta & \cos(\theta - 120^\circ) & \cos(\theta + 120^\circ) \\ -\sin\theta & -\sin(\theta - 120^\circ) & -\sin(\theta + 120^\circ) \\ \frac{1}{2} & \frac{1}{2} & \frac{1}{2} \end{bmatrix}. \tag{10}$$

The inverse transformation is expressed as

$$\mathbf{T}^{-1} = \begin{bmatrix} \cos\theta & -\sin\theta & 1 \\ \cos(\theta - 120^\circ) & -\sin(\theta - 120^\circ) & 1 \\ \cos(\theta + 120^\circ) & -\sin(\theta + 120^\circ) & 1 \end{bmatrix}. \tag{11}$$

For the stator and rotor of the WR-IM, θ of (10) and (11) is replaced by

$$\begin{aligned} \theta_s &= \omega_s t + \theta_0 = 2\pi f_s t + \theta_0 \\ \theta_r &= (\omega_s - \omega_r)t + \theta_0 = \omega t + \theta_0 = 2\pi(f_s - f_r)t + \theta_0 \end{aligned} \tag{12}$$

respectively, where t and θ_0 are the rotor position time and the initial rotor position, respectively. ω_s and ω_r are the stator and rotor angular velocities, respectively, and f_s and f_r are the grid supply and rotor frequencies, respectively. The slip frequency f of (12) for a p-pole pair motor is calculated from the rotor speed n_r as

$$f = (f_s - f_r) = \left(f_s - \frac{n_r p}{60}\right). \tag{13}$$

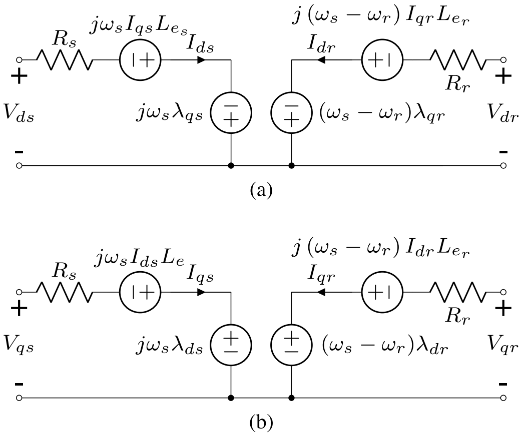

Fig. 1. (a) D- and (b) Q-axes equivalent circuit in the synchronously rotating reference frame in steady state of the WR-IM.

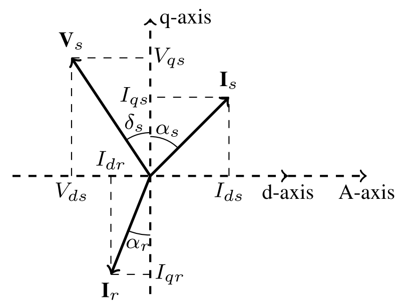

Fig. 2. DQ-axis phasor diagram of the WR-IM.

The transformed $\mathbf{T}$ equations of (5) in (7)–(9) result in

$$\begin{aligned} \mathbf{v}_{dqs} &= \mathbf{R}_s\mathbf{i}_{dqs} + \frac{d}{dt}\boldsymbol{\lambda}_{dqs} \mp \boldsymbol{\omega}_s\boldsymbol{\lambda}_{qds} \\ \mathbf{v}_{dqr} &= \mathbf{R}_r\mathbf{i}_{dqr} + \frac{d}{dt}\boldsymbol{\lambda}_{dqr} \mp (\boldsymbol{\omega}_s - \boldsymbol{\omega}_r)\boldsymbol{\lambda}_{qdr}. \end{aligned} \tag{14}$$

In steady state, the transformed voltage equations of (14) become

$$\begin{aligned} \mathbf{V}_{dqs} &= \mathbf{R}_s\mathbf{I}_{dqs} \mp \boldsymbol{\omega}_s\boldsymbol{\lambda}_{qds} \\ \mathbf{V}_{dqr} &= \mathbf{R}_r\mathbf{I}_{dqr} \mp (\boldsymbol{\omega}_s - \boldsymbol{\omega}_r)\boldsymbol{\lambda}_{qdr}. \end{aligned} \tag{15}$$

The voltage equations of (15), including the effect of the end-winding inductance L_e, which is given by

$$L_{e_{(s,r)}} = V_{(u)} m D_{(s,r)} (N_{(s,r)} q k_d k_{p(u)})^2 k_{e(p)} (10)^{-8} \tag{16}$$

where m is the number of phases and the shape factor $V_{(u)}$, distribution factor k_d, pitch factor k_p, and end-winding factor k_e explicitly given by Kamper [26], result in the DQ-axis equivalent circuits and phasor diagrams of Figs. 1 and 2, respectively. The core losses are not included in the equivalent circuit (by means of a core loss resistance) because these losses are lumped with mechanical losses as rotational losses.

The total DQ-axis flux linkages $\lambda_{qd_{(s,r)}}$ of (15) can be segregated into components and represented in matrix form given by

$$\boldsymbol{\lambda}_{dq_{(s,r)}} = \mathbf{L}_{(s,r)}\mathbf{I}_{dq_{(s,r)}} \tag{17}$$

as

$$\begin{bmatrix}\lambda_{ds}\\ \lambda_{qs}\\ \lambda_{dr}\\ \lambda_{qr}\end{bmatrix}=\begin{bmatrix}L_{ds} & M_{dsqs} & M_{dsdr} & M_{dsqr}\\ M_{qsds} & L_{qs} & M_{qsdr} & M_{qsqr}\\ M_{drds} & M_{drqs} & L_{dr} & M_{drqr}\\ M_{qrds} & M_{qrqs} & M_{qrdr} & L_{qr}\end{bmatrix}\begin{bmatrix}I_{ds}\\ I_{qs}\\ I_{dr}\\ I_{qr}\end{bmatrix} \tag{18}$$

where L and M represent the self and mutual inductances of the motor windings, respectively. In (17), $\mathbf{L}_{(s,r)}$ is the stator and rotor inductance matrix.

The performance equations of (15) can be modified by using (18) to become

$$\mathbf{V}=\mathbf{ZI} \tag{19}$$

where $\mathbf{V}$, $\mathbf{I}$ and $\mathbf{Z}$ are the voltage, current and impedance matrices given by

$$\mathbf{V}=[I_{ds} \quad I_{qs} \quad I_{dr} \quad I_{qr}] \tag{20}$$

$$\mathbf{I}=[I_{ds} \quad I_{qs} \quad I_{dr} \quad I_{qr}] \tag{21}$$

and (22), shown at the bottom of the page, respectively. It can be seen from the performance equation of (19) that knowing $\mathbf{V}$ and $\mathbf{Z}$ of (20) and (22), respectively, $\mathbf{I}$ of (21) can be calculated as

$$\mathbf{I}=\mathbf{Z}^{-1}\mathbf{V}. \tag{23}$$

Also following the transformed flux linkages $\boldsymbol{\lambda}_{dq_{(s,r)}}$ of (9), the general average total torque of the WR-IM is given by

$$T_t=\frac{3}{2}p(\lambda_{ds}I_{qs}-\lambda_{qs}I_{ds}). \tag{24}$$

The total torque can further be segregated into components by using the flux linkage components of (18) in (17) into the total torque equation of (24) to give the total torque as

$$T_t=T_r+T_s+T_m \tag{25}$$

where

$$\begin{aligned}T_r &= \frac{3}{2}p[(M_{dsqr}I_{qr}+M_{dsdr}I_{dr})I_{qs}\\ &\quad -(M_{qsdr}I_{dr}+M_{qsqr}I_{qr})I_{ds}]\\ T_s &= \frac{3}{2}p[(L_{ds}-L_{qs})I_{ds}I_{qs}]\\ T_m &= \frac{3}{2}p\big[M_{dq}\big(I_{qs}^2-I_{ds}^2\big)\big]\{M_{dsqs}=M_{qsds}=M_{dq}\}.\end{aligned} \tag{26}$$

In (25), the total torque T_t is expressed in terms of the rotor flux torque (T_r), saliency torque (T_s), and cross-magnetizing torque (T_m). T_r is due to the rotor-induced flux seen by the stator, T_s is due to the difference between the two D- and Q-axes stator inductances engendering in reluctance or saliency torque and T_m is due to the cross-magnetization between the D- and Q-axes. With regard to calculation of the torque, it is of great importance to understand that the torque of (24) does not include higher order permeance harmonics torques, i.e., the flux derivative terms have been neglected in (24).

Equations (23) and (25) form the basis of parameter and performance prediction of the WR-IM of the method described in Sections IV and V.

IV. FEA Computation of WR-IM Inductances

To calculate the inductance matrix $\mathbf{L}_{(s,r)}$ of (18) in (17), the total flux linkages $\boldsymbol{\lambda}_{dq_{(s,r)}}$ of (17) have to be segregated as in (18). To do so, the frozen permeability method [27]–[29], implemented in this paper for the WR-IM, is used to compute the flux linkage components.

In the method, a double excited non-linear FEA solution is used to determine the total transformed DQ-axis flux linkages $\boldsymbol{\lambda}_{dq_{(s,r)}}$ of (18) in (17). Thus, an initial current $\mathbf{I}_{dq_{(s,r)}}$ of (8) is set by current angles α_s and α_r of Fig. 2. The $\mathbf{I}_{dq_{(s,r)}}$ is inverse transformed to obtain phase current $\mathbf{i}_{\mathrm{abc}_{(s,r)}}$ as in (8), which is in turn used by the FEA package to calculate the phase flux linkage $\boldsymbol{\lambda}_{\mathrm{abc}_{(s,r)}}$. $\boldsymbol{\lambda}_{\mathrm{abc}_{(s,r)}}$ is inversely transformed to obtain the total DQ-axis flux linkages $\boldsymbol{\lambda}_{dq_{(s,r)}}$. The permeabilities of the elements of the FEA mesh are then frozen to preserve all the information about saturation in the motor on the stated load condition. Thus, by freezing the permeabilities the non-linear problem becomes a linear problem. In the instance of the WR-IM, four linear magnetostatic FEA solutions are necessary to calculate the DQ-axis flux linkage components.

The columns of the inductance matrix $\mathbf{L}_{(s,r)}$ of (18) in (17) are defined by

$$\begin{aligned}\mathbf{L}_{(s,r)_1} &= [L_{ds} \quad M_{qsds} \quad M_{drds} \quad M_{qrds}]^T\\ \mathbf{L}_{(s,r)_2} &= [M_{dsqs} \quad L_{qs} \quad M_{drqs} \quad M_{qrqs}]^T\\ \mathbf{L}_{(s,r)_3} &= [M_{dsdr} \quad M_{qsdr} \quad L_{dr} \quad M_{qrdr}]^T\\ \mathbf{L}_{(s,r)_4} &= [M_{dsqr} \quad M_{qsqr} \quad M_{drqr} \quad L_{qr}]^T.\end{aligned} \tag{27}$$

According to (18)

$$\begin{aligned}\boldsymbol{\lambda}_{dq_{(s,r)_1}} &= \mathbf{L}_{(s,r)_1}I_{ds}\\ \boldsymbol{\lambda}_{dq_{(s,r)_2}} &= \mathbf{L}_{(s,r)_2}I_{qs}\\ \boldsymbol{\lambda}_{dq_{(s,r)_3}} &= \mathbf{L}_{(s,r)_3}I_{dr}\\ \boldsymbol{\lambda}_{dq_{(s,r)_4}} &= \mathbf{L}_{(s,r)_4}I_{qr}.\end{aligned} \tag{28}$$

The flux linkages of (28) are determined from the four linear magnetostatic FEA solutions with single excitation of the DQ-axis currents as follows:

$$\begin{aligned}&\boldsymbol{\lambda}_{dq_{(s,r)_1}} \qquad \mathbf{I}=[I_{ds} \quad 0 \quad 0 \quad 0]^T\\ &\boldsymbol{\lambda}_{dq_{(s,r)_2}} \qquad \mathbf{I}=[0 \quad I_{qs} \quad 0 \quad 0]^T\\ &\boldsymbol{\lambda}_{dq_{(s,r)_3}} \qquad \mathbf{I}=[0 \quad 0 \quad I_{dr} \quad 0]^T\\ &\boldsymbol{\lambda}_{dq_{(s,r)_4}} \qquad \mathbf{I}=[0 \quad 0 \quad 0 \quad I_{qr}]^T.\end{aligned} \tag{29}$$

$$\mathbf{Z}=\left[\begin{bmatrix}(R_s-\omega_s M_{qsds}) & -\omega_s(L_{e_s}+L_{qs}) & -2\pi f_s M_{qsdr} & -2\pi f_s M_{qsqr}\\ \omega_s(L_{e_s}+L_{ds}) & (R_s+\omega_s M_{dsqs}) & 2\pi f_s M_{dsdr} & 2\pi f_s M_{dsqr}\\ -\omega M_{qrds} & -\omega M_{qrqs} & (R_r-\omega M_{qrdr}) & -\omega(L_{e_r}+L_{qr})\\ \omega M_{drds} & \omega M_{drqs} & \omega(L_{e_r}+L_{dr}) & (R_r+\omega M_{drqr})\end{bmatrix}\right] \tag{22}$$

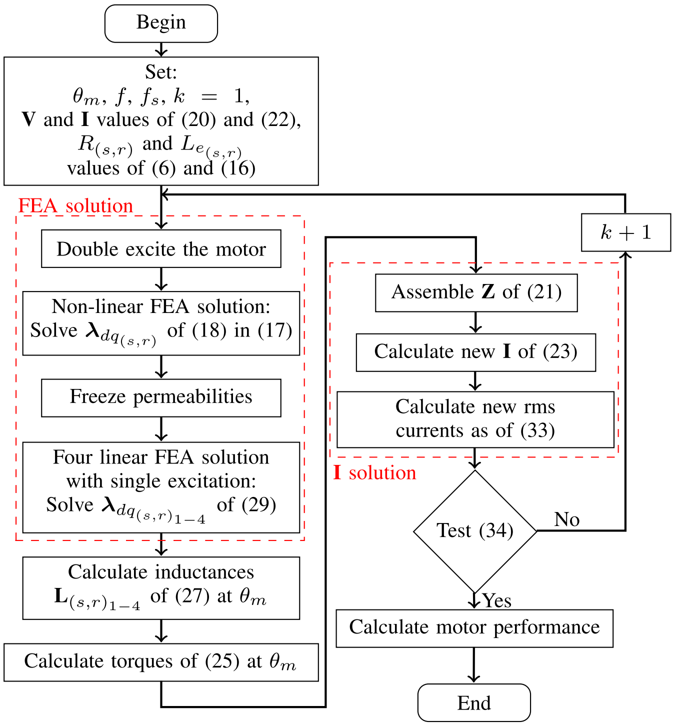

Fig. 3. Parameter and performance prediction flow-diagram of the WR-IM.

With the flux linkages of (29) known, the inductances of (27) using (28) are given by

$$\begin{aligned}\mathbf{L}_{(s,r)_1} &= \boldsymbol{\lambda}_{dq_{(s,r)_1}} I_{ds}^{-1}\\ \mathbf{L}_{(s,r)_2} &= \boldsymbol{\lambda}_{dq_{(s,r)_2}} I_{qs}^{-1}\\ \mathbf{L}_{(s,r)_3} &= \boldsymbol{\lambda}_{dq_{(s,r)_3}} I_{dr}^{-1}\\ \mathbf{L}_{(s,r)_4} &= \boldsymbol{\lambda}_{dq_{(s,r)_4}} I_{qr}^{-1}.\end{aligned} \tag{30}$$

It is of great significance to take note that the total DQ-axis non-linear FEA solution is equal to the sum of the four respective individual DQ-axis linear FEA solutions i.e.,

$$\boldsymbol{\lambda}_{dq_{(s,r)}} = \sum_{i=1}^{4} \boldsymbol{\lambda}_{dq_{(s,r)i}} = \sum_{i=1}^{4} \mathbf{T}(\theta_{(s,r)})\boldsymbol{\lambda}_{\mathrm{abc}_{(s,r)i}}. \tag{31}$$

V. Performance Computation of WR-IM

The WR-IM performance is computed following the electromagnetic model and inductance calculations presented in the previous sections. First the estimated impedance matrix $\mathbf{Z}$ of (22) at an initial estimated current matrix $\mathbf{I}$ of (21) is determined. With $\mathbf{Z}$ known, a new (updated) $\mathbf{I}$ is determined from (23) at a set voltage $\mathbf{V}$ according to (20). For example, by only considering a positive q-axis voltage ($\delta_s = 0$ of Fig. 2), the set $\mathbf{V}$ is given by

$$[V_{ds} \quad V_{qs} \quad V_{dr} \quad V_{qr}]^T = [0 \quad 325 \quad 0 \quad 0]^T. \tag{32}$$

An iterative technique is then employed to update $\mathbf{Z}$ at the updated $\mathbf{I}$ until *rms* values of $\mathbf{I}$ converge to a final value.

Fig. 3 shows the proposed calculation method (PCM) for the DQ-axis parameters and performance prediction with frozen permeabilities procedure. The variable θ_m is the identified mechanical rotor position angle. In Fig. 3, $k = 1, 2, \ldots, M$ is the convergence iterator where M is the number of iterations for the iterative technique termination. The current *rms* value of the k^{th} convergence iterator is calculated from the peak current value of (21) as

$$I_{rms_{(k)}} = \{0.5[I_{ds_{(k)}}^2 + I_{qs_{(k)}}^2]\}^{\frac{1}{2}} \quad k = 1, 2, \ldots, M. \tag{33}$$

The iterative technique is terminated when

$$I_{rms_{(k)}} - I_{rms_{(k-1)}} \leqslant \zeta \left(\frac{I_{rms_{(k)}} + I_{rms_{(k-1)}}}{2}\right) \tag{34}$$

where ζ is the fraction tolerance in the current value and $I_{rms_{(k)}}$ and $I_{rms_{(k-1)}}$ are the start and final current values of one iteration. The DQ-axis current and torque values can also be used as function values for the iteration termination as in (34). Finally, note that the PCM of Fig. 3 for the performance computation of the WR-IM is done at a single rotor position, an aspect which is considered later in this paper.

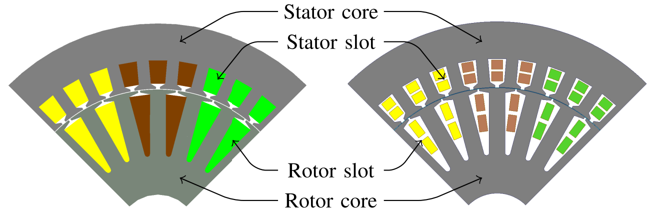

Fig. 4. IH-FE (left) and AM-FE (right) 2-D axial view models of the WR-IM.

VI. Case Study Computation of WR-IM

In this section, performance and parameter computed results are given of an unskewed WR-IM using the PCM implemented in an in-house static FEA (IH-FE) software package. The computed results are validated using a commercial transient FEA package, Ansoft/Maxwell (AM-FE). Fig. 4 shows 2-D IH-FE and AM-FE pole section simulation models of a four pole WR-IM with 36 stator and 24 rotor slots. The dimensions and parameters of the motor models of Fig. 4 are tabulated in Table I.

A. Performance Computation Results

Fig. 5 shows (a) *rms* current values of (33) $I_{(33)}^{f}$ and (b) torque values of (25) $T_{(25)}^{f}$ versus the convergence iterator k of Fig. 3 for 15 iterations (i.e., $M = 15$). Different slip frequency values (i.e., $f = 0$, 1.5, and 50 Hz) shown on the superscript of the performance motor variables are used to demonstrate the PCM behavior at diverse conditions. At a set voltage matrix $\mathbf{V}$ of (32), the results here show a converging behavior which indicates an opportunity for a performance solution at $\mathbf{V}$ and f. It is shown that it takes only up to six iterations to obtain a solution to the motor performance independent of f.

B. Parameter Computation Results

This section presents parameter results versus rotor position using the PCM for the current solution in Fig. 5 at $f = 1.5$ Hz (i.e., $n_r = 1\ 455$ r/min) and $k = 6$. Fig. 6 shows

TABLE I

DIMENSION AND PARAMETER VALUES OF THE WR-IM

Dimension description	**Stator**	**Rotor**	**Units**
Outer diameter	210	144.4	(mm)
Inner diameter	145	40	(mm)
Slot opening height	1	1	(mm)
Slot wedge height	1.5	1.5	(mm)
Slot height	11.65	29.3	(mm)
Slot opening width	2	1	(mm)
Lower slot opening width	7.14	2.7	(mm)
Upper slot opening width	9.18	10.4	(mm)
Teeth width	5.95	8.61	(mm)
Stack length	120	120	(mm)
Air gap length	0.305		(mm)
Parameter description			
Phase resistance	1.26	0.73	(Ω)
End-winding inductance	0.01	0.01	(H)
Turns per slot	24	36	-
Rated frequency	50	48.5	(Hz)
Rated phase voltage Y connection	230	0	(V)
Rated phase current	6.8	5.9	(A)
Rated Power	3.4		(kW)

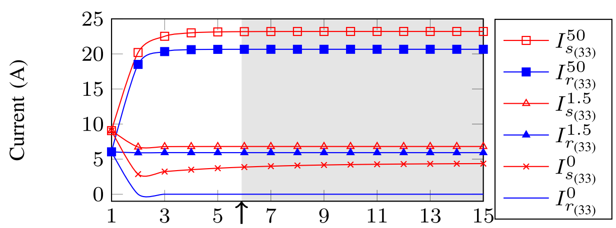

(a)

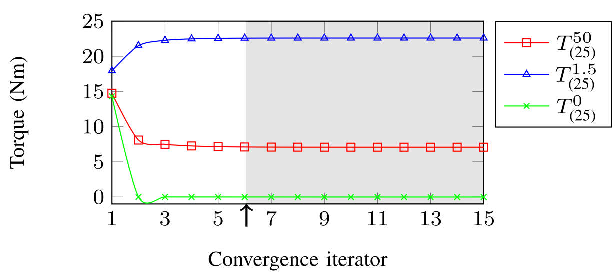

(b)

Fig. 5. (a) *rms* current and (b) torque values versus convergence iterator at slip frequencies of 0, 1.5 and 50 Hz.

the non-linear IH-FE solutions of total flux linkages of (17), also equal to the sum of the segregated flux linkages of (29) in (31). Fig. 7 shows the WR-IM self and mutual inductances values of (27) versus rotor position. These inductances are computed as of (30) from the segregated DQ-axis flux linkage components of (29). In Fig. 7(b), the results of only two mutual cross-coupling inductances are shown as an example. The results of M_{dsdr} and M_{qsqr} are not shown since they are equal to M_{drds} and M_{qrqs}, respectively. Fig. 8 shows the segregated torque components of (25) $T_{(25)}$ (i.e., T_t) and the IH-FE torque $T_{(IH)}$ versus rotor position.

The parameter and torque performance results of Figs. 7 and 8 with fixed DQ-axis currents show very little variation with rotor position for the unskewed motor. However, $T_{(IH)}$ has a high torque ripple as shown because it is the actual FE-calculated rotor position torque.

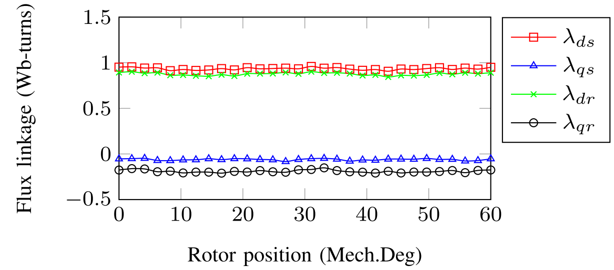

Fig. 6. Total flux linkages from the non-linear FE solution versus rotor position according to (9).

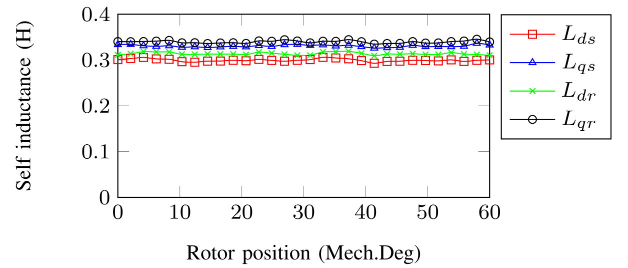

(a)

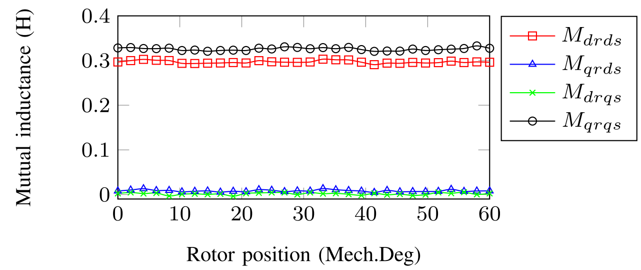

(b)

Fig. 7. DQ-axis (a) self and (b) mutual inductances versus rotor position.

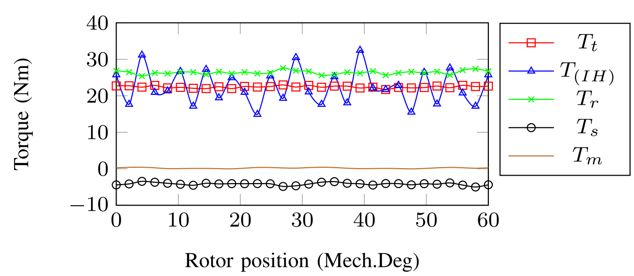

Fig. 8. Torque versus rotor position.

C. PCM Solution at Different Rotor Positions

As mentioned earlier, the results of Figs. 7 and 8 versus rotor position are with fixed DQ-currents. The question is how will the PCM current and torque solution of Fig. 3 vary with the designer's choice of rotor position, θ_m. Fig. 9 shows these PCM results versus the designer's choice of θ_m, with slip frequency a parameter. For the unskewed motor, the results show that the PCM predicts the current and torque at any choice of θ_m without introducing a weighty error.

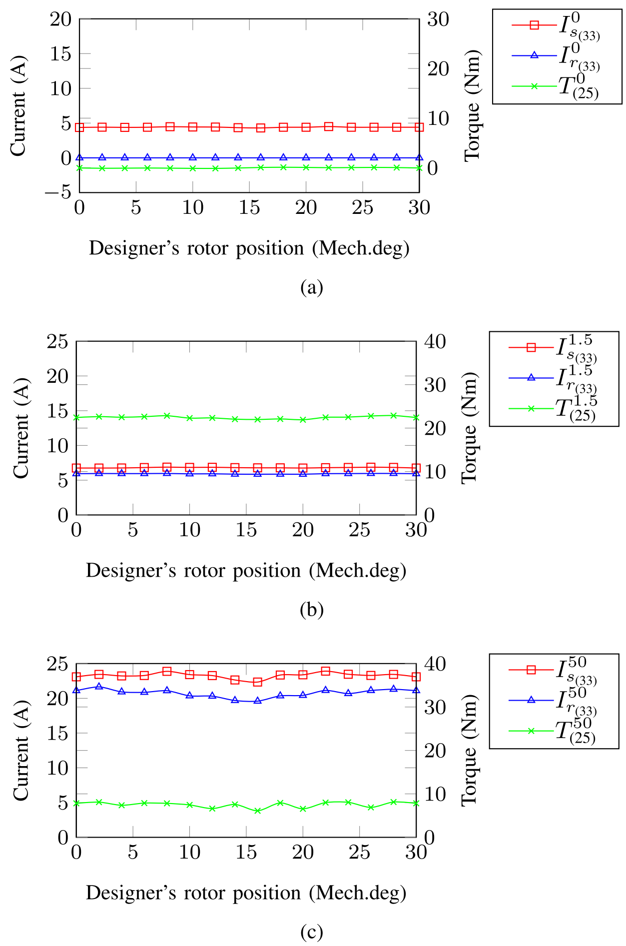

Fig. 9. *rms* current and torque versus rotor position with slip frequencies of (a) 0, (b) 1.5, and (c) 50 Hz.

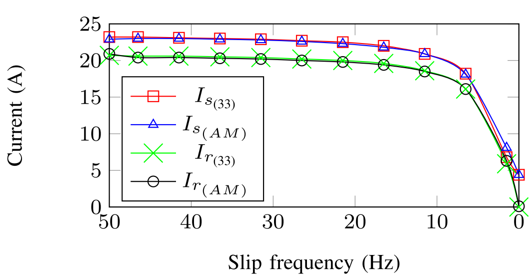

Fig. 10. PCM and AM-FE *rms* current versus slip frequency.

D. Validation of PCM Results

To validate the PCM of Fig. 3, the AM-FE model of the WR-IM of Fig. 4 is simulated. Fig. 10 shows the PCM and AM-FE stator and rotor *rms* currents (i.e., $I_{(s,r)(33)}$, $I_{(s,r)(AM)}$) versus slip frequency, respectively. Fig. 11 also shows the IH-FE, and AM-FE average and PCM torques (i.e., $\overline{T}_{(IH)}$, $\overline{T}_{(AM)}$, $T_{(25)}$) versus slip frequency, respectively. The obtained results using the PCM are in excellent agreement with those obtained from the transient AM-FE and static IH-FE solutions.

VII. Discussion of Simulation Results

From the PCM of Fig. 3, a single iteration ($M = 1$) requires 1 × non-linear plus 4 × linear FE solutions for parameter and performance prediction. Since the linear FE solution with

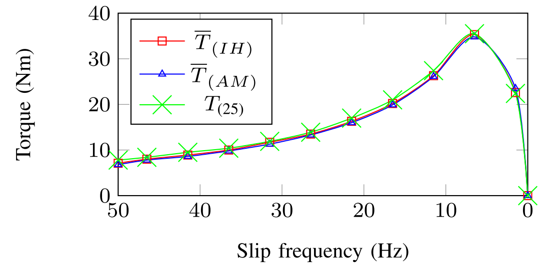

Fig. 11. IH-FE, AM-FE, and PCM torque versus slip frequency.

frozen permeabilities is relatively very fast, the time taken for the 4 × linear FE solutions can be neglected. Furthermore, for convergence from the results of Fig. 5, only $M = 6$ static non-linear FE solutions are needed for accurate parameter and performance prediction.

In order to have a quantitative comparison of the computational time, the steady state *rms* stator current solutions of the AM-FE and PCM at 50 Hz (stand still) and 1.5 Hz slip frequencies have been simulated. On a 2.93 GHz CPU with 12 GB RAM Intel(R) Core i7 computer, the execution times were found in this case to be 1833 and 166 s, respectively, for the AM-FE and PCM methods. Hence the PCM method is eleven times faster than the AM-FE method, which is extremely important when it comes to design optimization. Furthermore, the accessibility of the actual motor parameters (e.g., inductances) from the analysis using the total flux linkages gives the PCM a major advantage in the precise modeling of the electrical machine. Note has to be taken that any FEA package (commercial or non-commercial) can be utilized in the PCM as long as the package can execute static FE solutions and is capable of freezing the core-element permeabilities.

The PCM includes the effects of saturation saliency and cross-magnetization on the WR-IM circuit parameters [30]–[32]. However, it was found, among others from the results of Fig. 7, that the small WR-IM does not suffer significantly from the effect of cross-magnetization. Hence, the motor is easily analyzed on orthogonal axes assuming that they are decoupled. The inductance matrix of (18) in (17) can then classically be adapted as [2], [33]

$$\mathbf{L}_{(s,r)} \approx \begin{bmatrix} L_{ds} & 0 & M_d & 0 \\ 0 & L_{qs} & 0 & M_q \\ M_d & 0 & L_{dr} & 0 \\ 0 & M_q & 0 & L_{qr} \end{bmatrix} \tag{35}$$

where $M_d = M_{drds} = M_{dsdr}$ and $M_q = M_{qrqs} = M_{qsqr}$. However, it is wrong to assume that the corresponding DQ-axis self and mutual inductances of the stator and rotor are equal as illustrated in (35). With the simplified inductance matrix of (35) the torque components of (26) in (25) simplifies to

$$\begin{aligned} T_r &= \frac{3}{2}p(M_d I_{dr} I_{qs} - M_q I_{qr} I_{ds}) \\ T_s &= \frac{3}{2}p[(L_{ds} - L_{qs}) I_{ds} I_{qs}] \\ T_m &= 0 \end{aligned} \tag{36}$$

as is also shown by the torque components in Fig. 8.

VIII. Conclusion

An implementation method on modeling the WR-IM, essentially predicting motor parameters and performances at any slip speed, is described in this paper. The PCM is found to be successful in that it determines accurate and fast solutions for performance prediction. Hence, the method is extremely suited, amongst others, to the design optimization of the WR-IM.

Acknowledgment

This work was supported by the European Horizon 2020.

References

[1] M. Mabhula and M. Kamper, "Improving starting torque quality of wound-rotor induction motor for geared fan loads," in *Proc. Southern African Univ. Power Eng. Conf. (SAUPEC)*, Stellenbosch, South Africa, Jan./Feb. 2017, pp. 607–612.

[2] S. Umans, A. Fitzgerald, and C. Kingsley, *Electric Machinery*, 7th ed. New York, NY, USA; McGraw-Hill, 2013.

[3] A. Demenko and L. Nowak, "Finite element analysis of saturation effects in a squirrel cage electrical machine," *COMPEL, Int. J. Comput. Math. Elect. Electron. Eng.*, vol. 15, no. 4, pp. 88–95, 1996.

[4] B. Amin, *Induction Motors: Analysis and Torque Control*. New York, NY, USA: Springer, 2001.

[5] S. Niu, S. L. Ho, and W. Fu, "Fast computation of torque-speed characteristics of induction machines," in *Proc. IEEE Magn. Conf. (INTERMAG)*, May 2015, p. 1.

[6] J. Rolek and G. Utrata, "A methodology for electromagnetic parameter estimation of an induction motor equivalent circuit based on the load curve test," in *Proc. Int. Symp. Electr. Mach. (SME)*, Jun. 2017, pp. 1–6.

[7] P. Farhadi, M. Gheydi, F. Abdolahnejad, and A. J. Pireivatloo, "Simultaneous improvement of distortion of current and torque in induction motor by optimization of linkage flux distortion," in *Proc. 8th Power Electron., Drive Syst. Technol. Conf. (PEDSTC)*, Feb. 2017, pp. 73–77.

[8] E. E. M. Rashad, "Effect of parameters on sub-synchronous operation of series-connected wound-rotor induction motor," in *Proc. IEEE Int. Conf. Power Energy (PECon)*, Nov. 2016, pp. 534–539.

[9] M. Mengoni, L. Zarri, G. Rizzoli, A. Tani, Y. Gritli, and M. J. Duran, "Use of field harmonics in multiphase induction motor drives for on-line parameter estimation," in *Proc. IEEE Workshop Electr. Mach. Design, Control Diagnosis (WEMDCD)*, Apr. 2017, pp. 222–227.

[10] S.-H. Lee, A. Yoo, H.-J. Lee, Y.-D. Yoon, and B.-M. Han, "Identification of induction motor parameters at standstill based on integral calculation," *IEEE Trans. Ind. Appl.*, vol. 53, no. 3, pp. 2130–2139, May/Jun. 2017.

[11] I. Boldea and S. Nasar, *The Induction Machine Handbook* (Electric Power Engineering Series). Boca Raton, FL, USA: CRC Press, 2010.

[12] W. N. Fu, S. L. Ho, H. L. Li, and H. C. Wong, "A multislice coupled finite-element method with uneven slice length division for the simulation study of electric machines," *IEEE Trans. Magn.*, vol. 39, no. 3, pp. 1566–1569, May 2003.

[13] T. W. Preston, A. B. J. Reece, and P. S. Sangha, "Induction motor analysis by time-stepping techniques," *IEEE Trans. Magn.*, vol. MAG-24, no. 1, pp. 471–474, Jan. 1988.

[14] W. N. Fu and S. L. Ho, "Extension of the concept of windings in magnetic field—Electric circuit coupled finite—Element method," *IEEE Trans. Magn.*, vol. 46, no. 6, pp. 2119–2123, Jun. 2010.

[15] A. Salah, Y. Guo, and D. Dorrell, "Impedance matrix analysis technique in wound rotor induction machines including general rotor asymmetry," in *Proc. 42nd Annu. Conf. IEEE Ind. Electron. Soc. (IECON)*, Oct. 2016, pp. 1821–1826.

[16] S. Mezani, T. Hamiti, L. Belguerras, T. Lubin, and C. Gerada, "Computation of wound rotor induction machines based on coupled finite elements and circuit equation under a first space harmonic approximation," *IEEE Trans. Magn.*, vol. 52, no. 3, Mar. 2016, Art. no. 8102204.

[17] A. C. Smith, S. Williamson, and J. R. Smith, "Transient currents and torques in wound-rotor induction motors using the finite-element method," *Proc. Inst. Elect. Eng. Elect. Power Appl.*, vol. 137, no. 3, pp. 160–173, May 1990.

[18] Y. Ouazir, N. Takorabet, R. Ibtiouen, and M. Benhaddadi, "Time-stepping FE analysis of cage induction motor with air-gap interface coupling taking into account phase-belt harmonics," *IEEE Trans. Magn.*, vol. 45, no. 3, pp. 1384–1387, Mar. 2009.

[19] K. Yamazaki, R. S. M. Nuka, and M. Masegi, "Characteristics improvement of claw-pole alternators by reducing armature reaction," in *Proc. IEEE Int. Electr. Mach. Drives Conf. (IEMDC)*, May 2017, pp. 1–6.

[20] G. Vinsard and B. Laporte, "A new formulation for induction machine computation," *IEEE Trans. Magn.*, vol. 30, no. 5, pp. 3693–3696, Sep. 1994.

[21] N. Takorabet, B. Laporte, and S. Mezani, "An approach to compute saturated induction motors in steady state," in *Proc. IEEE Int. Electr. Mach. Drives Conf. (IEMDC)*, vol. 3. Jun. 2003, pp. 1646–1650.

[22] H. De Gersem and K. Hameyer, "Air-gap flux splitting for the time-harmonic finite-element simulation of single-phase induction machines," *IEEE Trans. Magn.*, vol. 38, no. 2, pp. 1221–1224, Mar. 2002.

[23] G. Vinsard and B. Laporte, "An analysis of the first harmonic method to compute induction motors," *IEEE Trans. Magn.*, vol. 31, no. 3, pp. 2162–2165, May 1995.

[24] S. Mezani, N. Takorabet, and B. Laporte, "Saturation and space harmonics in the complex finite element computation of induction motors," *IEEE Trans. Magn.*, vol. 41, no. 5, pp. 1460–1463, May 2005.

[25] T. J. Flack and A. F. Volschenk, "Computational aspects of time-stepping finite-element analysis using an air-gap element," in *Proc. Int. Conf. Electr. Mach. (ICEM)*, vol. 3. 1994, pp. 158–163.

[26] M. Kamper, "Design optimisation of cageless flux barrier rotor reluctance synchronius machine," Ph.D. dissertation, Dept. Elect. Electron., Stellenbosch Univ., Stellenbosch, South Africa, Dec. 1996.

[27] M. Mabhula and M. J. Kamper, "Saliency and mutual inductance effect in cylindrical wound-rotor synchronous motor," in *Proc. IEEE Workshop Electr. Mach. Design, Control Diagnosis (WEMDCD)*, Apr. 2017, pp. 152–157.

[28] J. A. Walker, D. G. Dorrell, and C. Cossar, "Flux-linkage calculation in permanent-magnet motors using the frozen permeabilities method," *IEEE Trans. Magn.*, vol. 41, no. 10, pp. 3946–3948, Oct. 2005.

[29] J. K. Tangudu, T. M. Jahns, A. M. El-Refaie, and Z. Q. Zhu, "Segregation of torque components in fractional-slot concentrated-winding interior PM machines using frozen permeability," in *Proc. IEEE Energy Convers. Congr. Expo. (ECCE)*, Sep. 2009, pp. 3814–3821.

[30] J. E. Brown, K. P. Kovacs, and P. Vas, "A method of including the effects of main flux path saturation in the generalized equations of A.C. machines," *IEEE Trans. Power App. Syst.*, vol. PAS-102, no. 1, pp. 96–103, Jan. 1983.

[31] E. Levi, "Impact of cross-saturation on accuracy of saturated induction machine models," *IEEE Trans. Energy Convers.*, vol. 12, no. 3, pp. 211–216, Sep. 1997.

[32] M. Say, *Alternating Current Machines* (Engineering). Hoboken, NJ, USA: Wiley, 1983.

[33] A. Trzynadlowski, *Control of Induction Motors* (Engineering). New York, NY, USA: Elsevier, 2000.

Mkhululi Mabhula received the B.Eng. degree from Stellenbosch University, Stellenbosch, South Africa, in 2016. He is currently pursuing the master's degree in electrical machine design.

His current research interest includes the design optimization and control of electrical machines.

Maarten J. Kamper received the M.Sc. (Eng) and Ph.D.(Eng) degrees in engineering from the University of Stellenbosch, Stellenbosch, South Africa, in 1987 and 1996, respectively.

Since 1989, he has been with the Department of Electrical and Electronics Engineering, University of Stellenbosch, where he is currently a Professor of electrical machines and drives. His current research interests include the design optimization and control of electrical machines, currently with a focus on wind generators and industrial and electrical vehicle drives.

Prof Dr. Kamper is an Associate Editor of the Electric Machine Committee of the IEEE Transactions on Industry Applications. He also serves on the Steering Committee of the International Conference on Electrical Machines (ICEM).